Journal of
Materials Chemistry C

Materials for optical, magnetic and electronic devices

Accepted Manuscript

This article can be cited before page numbers have been issued, to do this please use: G. Kim, M. Kim, B. J. Moon, G. Moon, T. Kim, S. Ryu and S. H. Lee, *J. Mater. Chem. C*, 2026, DOI: 10.1039/D5TC04393J.

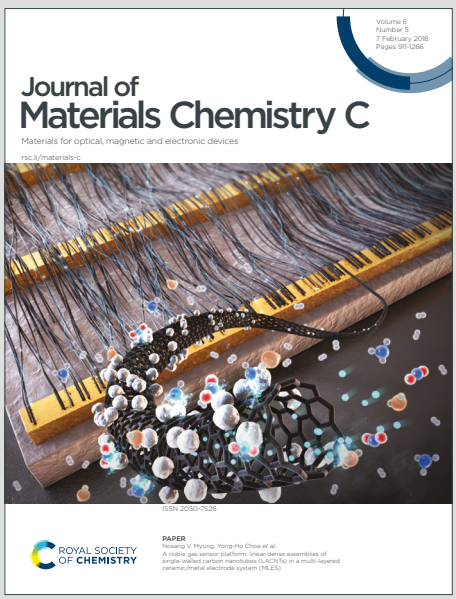

ROYAL SOCIETY OF CHEMISTRY

rsc.li/materials-c

View Article Online
DOI: 10.1039/D5TC04393J

ARTICLE

Comparative Optical Characterization of $CsPbBr_3$ Quantum Dots and CVD-Grown $CsPbBr_3$ Mircoplates

Received 00th January 20xx,
Accepted 00th January 20xx

DOI: 10.1039/x0xx00000x

Ga-Eun Kim,[a] Minjin Kim,[a] Byung Joon Moon,[b] Geol Moon,[c] Tae-Wook Kim,[d] Sang-Wan Ryu,[c] and Sang Hyun Lee[a,*]

We systematically investigate the influence of morphology on exciton dynamics and bandgap behavior in all-inorganic $CsPbBr_3$ nanostructures by comparing colloidal quantum dots (QDs) and chemical vapor deposition (CVD)-grown microplates. Despite their identical composition, the two forms exhibit markedly different optical characteristics due to variations in dimensionality, crystallinity, and surface/interface conditions. Steady-state and temperature-dependent photoluminescence (PL) spectroscopy, supported by structural analysis, reveals a quantum confinement-induced blueshift and shorter exciton lifetime in QDs, whereas microplates display sharper emission, longer carrier lifetimes, and enhanced coupling with lattice phonons. Notably, temperature-induced PL shifts are deconvoluted into thermal expansion and electron–phonon interaction components using a one-oscillator model, showing a stronger thermomechanical response in microplates due to substrate-induced strain and larger volume. Interestingly, the exciton binding energy is higher in microplates (46.3 meV) than in QDs (33.9 meV), likely due to surface defects and dielectric screening effects in ligand-capped QDs. These findings clarify the distinct role of morphology in governing exciton recombination, phonon coupling, and optical stability, offering new insights for the rational design of perovskite-based optoelectronic devices.

Introduction

Halide perovskites, especially cesium lead halides ($CsPbX_3$, X = Cl, Br, I), have attracted considerable interest for use as next-generation optoelectronic materials owing to their exceptional photophysical properties [1-4]. Among these materials, $CsPbBr_3$ is a leading candidate for light-emitting and photodetection applications because of its direct bandgap, high photoluminescence quantum yield, high oscillator strength, and excellent thermal stability [5,6]. These properties arise from the low-dimensional perovskite crystal structure and favorable electronic band dispersion of $CsPbBr_3$, which promote efficient excitonic transitions and radiative recombination [7,8].

Notable features of the optical behavior of $CsPbBr_3$ are its strong excitonic nature and its ability to strongly couple with phonons. At low temperatures, photoluminescence (PL) emission is dominated by bound and free excitons, with the optical characteristics being modulated by native point defects and intrinsic lattice disorder [9,10]. Carrier-phonon interactions lead to phonon-assisted recombination processes and multiphonon relaxation, especially through Fröhlich-type coupling with longitudinal optical phonons [11,12]. Temperature-dependent PL shifts observed in $CsPbBr_3$ nanocrystals and films have been attributed to lattice thermal expansion, exciton–phonon coupling, and phase transitions [13–15]. Despite the identical composition of $CsPbBr_3$, its optical behavior strongly depends on morphology, which is closely linked to dimensionality and the synthesis route. Dimensional confinement, surface passivation, dielectric environment, and interfacial strain all vary with dimensionality and growth conditions [16–18]. While $CsPbBr_3$ QDs offer size-tunable emission and strong confinement effects, they also suffer from high surface recombination and altered exciton–phonon coupling due to ligand screening [19]. By contrast, chemical vapor deposition (CVD)-grown $CsPbBr_3$ have extended crystalline domains and coherent interfaces with the substrate, and hence provide a contrasting platform to investigate excitonic recombination and phonon interactions [20,21]. Recently, Z. Su *et al.* reported lasing behavior with fast decay in well-faceted $CsPbBr_3$ nanoplates grown by CVD [22]. Furthermore, it has been demonstrated that the redshift of the bandgap can arises from reduced interfacial stress, while the enhanced carrier lifetime results from suppressed edge trapping and a lower density of surface trap states in vertically grown $CsPbBr_3$ nanostructures compared with their horizontally grown counterparts [23]. Despite these fundamental differences in the representative two growth conditions, a systematic and quantitative comparison of the optical

[a] School of Chemical Engineering, Chonnam National University, 77 Yongbong-ro, Buk-gu, Gwangju 61186, Republic of Korea.
[b] Functional Composite Materials Research Center, Institute of Advanced Composite Materials, Korea Institute of Science and Technology, Jeollabuk-do 55324, Republic of Korea
[c] Department of Physics, Chonnam National University, 77 Yongbong-ro, Buk-gu, Gwangju 61186, Republic of Korea
[d] Department of Flexible and Printable Electronics, LANL-JBNU Engineering Institute-Korea, Jeonbuk National University, 567 Baekje-daero, Deokjin-gu, Jeonju 54896, Republic of Korea
† Footnotes relating to the title and/or authors should appear here.
Supplementary Information available: [details of any supplementary information available should be included here]. See DOI: 10.1039/x0xx00000x

View Article Online
DOI: 10.1039/D5TC04051

characteristics of $CsPbBr_3$ QDs and CVD-grown $CsPbBr_3$ microstructures has not yet been reported.

In this work, we systematically investigated the optical properties of $CsPbBr_3$ QDs and CVD-grown $CsPbBr_3$ microplates by using steady-state and temperature-dependent PL spectroscopy. By analyzing key parameters such as emission peak energy, spectral linewidth, carrier lifetime, and phonon coupling strength, we establish clear correlations between morphology, dimensionality, and the temperature-dependent optical response. Our findings provide important insights into exciton dynamics and lattice interactions in halide perovskites and offer guidance for the rational design of perovskite structures in optoelectronic applications.

Experimental

Synthesis of $CsPbBr_3$ QDs

First, a Cs-oleate solution required for hot-injection was prepared by loading Cs_2CO_3 (0.250 g), 10 mL of 1-octadecene (ODE), and 1 mL of oleic acid (OA) into a three-necked flask [24,25]. The mixture was degassed at 70 °C under vacuum to eliminate moisture and oxygen, then purged with nitrogen and heated to 120 °C. The temperature was further raised to 150 °C to ensure that the reaction of Cs_2CO_3 with OA was complete. Once Cs_2CO_3 had fully dissolved, the Cs-oleate solution was stored at 105 °C until it was used for hot-injection. The $PbBr_2$ precursor was prepared by dissolving $PbBr_2$ (0.207 g) in 15 mL of ODE in a single-necked flask. The solution underwent vacuum degassing at 70 °C, followed by nitrogen purging at 120 °C. OA and oleylamine (OAm) were then introduced, and the mixture was stirred for 10 min and subsequently heated to 150 °C for final precursor formation. With both precursors ready, the preheated Cs-oleate solution was rapidly injected into the 150 °C $PbBr_2$ solution. After 10 s of reaction, the mixture was quenched by cooling. The product was isolated through centrifugation, redispersed in hexane, and centrifuged again to remove residual unreacted materials and by-products. Finally, $CsPbBr_3$ QDs, in powder form, were collected and dried under vacuum.

Synthesis of $CsPbBr_3$ microplates

$CsPbBr_3$ powder, synthesized via hot-injection and thoroughly dried, served as a single-source precursor in CVD. The powder was loaded into a quartz boat, which was then placed in the hot zone of the furnace; a *c*-Al_2O_3 substrate cleaned with organic solvents was positioned downstream. After evacuating the furnace, we purged the system with argon for 30 min to remove residual contaminants. The furnace was then ramped to 400 °C and held at the temperature for 10 min to facilitate nanoplate growth. Finally, the reactor was allowed to cool naturally to room temperature under continuous argon flow.

Characterizations

The crystal structures of the $CsPbBr_3$ QDs and microplates were characterized by X-ray diffraction (XRD) using an EMPyrean diffractometer (PANalytical), and the surface morphology was examined by scanning electron microscopy (SEM) performed using a Hitachi SU5000 system. High-resolution structural images and elemental distributions were obtained using spherical-aberration-corrected scanning transmission electron microscopy (Cs-STEM, JEM-ARM200F, JEOL) operated at an acceleration voltage of 200 kV; the STEM system was equipped with an energy-dispersive X-ray spectroscopy (EDS) detector. X-ray photoelectron spectroscopy (XPS) was carried out on a Thermo Scientific K-Alpha$^+$ spectrometer equipped with a monochromatic Al Kα X-ray source. Steady-state PL spectra were measured with a Horiba iHR-320 monochromator using a 442 nm He–Cd laser (IK5552R-F, Kimmon Electric) as the excitation source. Photoluminescence quantum yield (PLQY) measurements were performed using a Quanta-Phi integrating sphere coupled with a Horiba Fluorolog spectrophotometer. For temperature-dependent PL measurements, $CsPbBr_3$ QD films were fabricated by drop-casting the prepared $CsPbBr_3$ solution onto SiO_2/Si substrates and gently drying at low temperature to preserve the structural integrity of the QDs. The samples were mounted on the cold finger of a closed-cycle helium cryostat (model RF273SA, Aisin Seiki Co.) equipped with optical windows. To prevent surface condensation and ensure thermal insulation, the cryostat chamber was evacuated to a high vacuum prior to cooling. The sample temperature was precisely varied and stabilized from 10 K to 300 K using a Lake Shore 335 temperature controller. Time-resolved PL (TRPL) was employed to probe carrier dynamics, with the second harmonic (400 nm) of a femtosecond Ti:sapphire laser (Mai Tai, Spectra-Physics; pulse width: ~100 fs; repetition rate: 80 MHz) serving as the excitation source.

Results and discussion

To investigate the structural and compositional characteristics of the $CsPbBr_3$ nanostructures, we conducted TEM and SEM analyses; representative images are shown in Fig. Fig. 1 (and in Figs.S1 and S2). A low-magnification TEM image of the $CsPbBr_3$ QDs shows a uniform morphology and a well-defined cubic structure with an average size of approximately 10 nm. The inset of Fig. 1(a) depicts a high-resolution TEM image that clearly shows lattice fringes with a spacing of 0.58 nm, corresponding to the (100) planes of cubic $CsPbBr_3$.

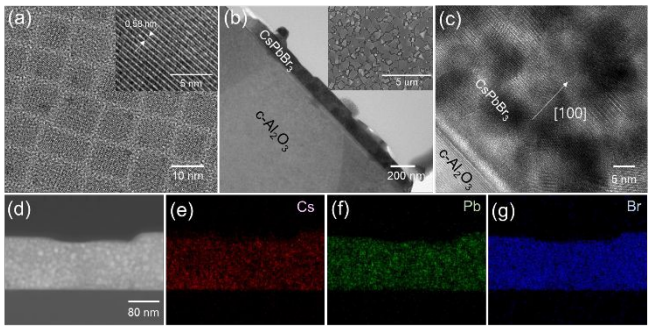

Figure 1. (a) TEM image of $CsPbBr_3$ QDs; the inset shows a high-resolution TEM image of QDs with a lattice spacing of 0.58 nm. (b) Cross-sectional TEM image of $CsPbBr_3$ microplates

View Article Online
DOI: 10.1039/D5TC04031

grown on a *c*-Al_2O_3 substrate via CVD; the inset shows a top-view SEM image depicting densely packed microplates. (c) High-magnification TEM image of the interface between a $CsPbBr_3$ nanoplate and the *c*-Al_2O_3 substrate. (d) Low-magnification cross-sectional TEM image of a nanoplate. EDS elemental mapping of (e) Cs, (f) Pb, and (g) Br is also shown.

To determine the morphology and examine the interfaces of the $CsPbBr_3$ microplates grown via CVD, we obtained a cross-sectional TEM image (Fig. 1(b)). The $CsPbBr_3$ microplates formed a homogeneous layer with a thickness of approximately 100 nm and a width of a few micrometers on the *c*-Al_2O_3 substrate. The inset of Fig. 1(b) shows a top-view SEM image which the microplates appear densely packed with a continuous and planar surface morphology. The high-resolution TEM image of the interface in Fig. 1(c) further confirms the uniform growth of a $CsPbBr_3$ nanoplate on the *c*-Al_2O_3 substrate. Lattice fringes across the interface were clearly resolved, and the growth direction of $CsPbBr_3$ on (0001) Al_2O_3 is identified as [002], indicating a well-ordered and coherent interface (Fig. S1). Figure 1(d) shows a low-magnification cross-sectional TEM image of a nanoplate, used for elemental analysis. The EDS elemental mapping in Figs. 1(e–g) shows that Cs, Pb, and Br were homogeneously distributed throughout the nanoplate, confirming that the $CsPbBr_3$ phase has a uniform composition.

The crystallographic phase and structural quality of the synthesized $CsPbBr_3$ structures were characterized using XRD, and resulting diffraction patterns are shown in Fig. 2. The diffraction patterns (black and blue curves) of $CsPbBr_3$ QDs and microplates showed distinct, sharp, and well-defined peaks, indicating high crystallinity. These peaks match well with those of the reference pattern for cubic-phase $CsPbBr_3$ (PDF# 54-0752, shown in red), confirming the formation of a perovskite structure without any detectable secondary phase [26]. A significant difference in crystallite size is evident from the full width at half-maximum (FWHM) of the (100) diffraction peak, which is 0.84º for QDs, considerably greater than value of 0.1 º for the microplates. When the crystallite size decreases from bulk to nanoscale dimensions, the XRD peaks broaden, mainly due to the restricted number of reflection planes in the small

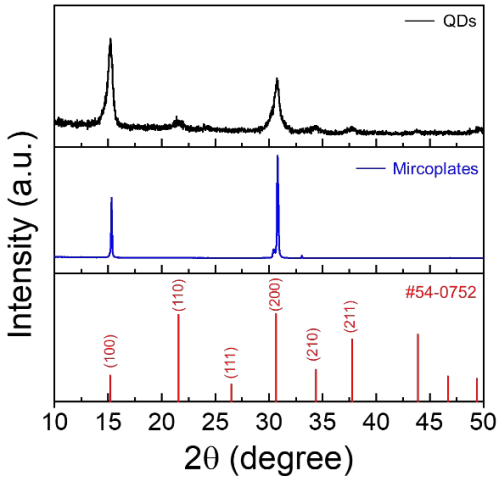

crystallite size and stress/strain [27, 28] From the Scherrer equation [29], the average size of the QDs was estimated to be approximately 11 nm, which was in good agreement with that determined from TEM analysis (Fig. 1(a)).

Figure 2. XRD patterns of $CsPbBr_3$ QDs and microplates along with the standard peaks of a cubic $CsPbBr_3$ crystal (PDF No. 54-0752).

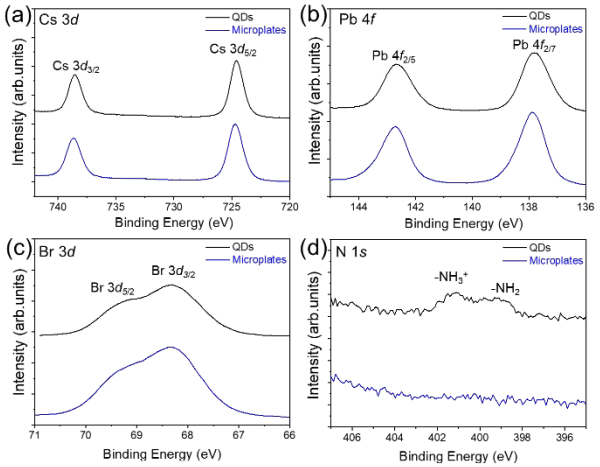

Figure 3. High-resolution XPS spectra of $CsPbBr_3$ QDs (black) and microplates (blue) for (a) Cs *3d*, (b) Pb *4f*, (c) Br *3d*, and (d) N *1s*, respectively.

XPS measurements were carried out to clarify the surface chemistry of the $CsPbBr_3$ QDs and microplates. Quantitative analysis of the peak areas indicates that the Cs:Pb:Br ratios of the QDs and microplates are close to the nominal 1:1:3 stoichiometry, suggesting that the overall halide content is well preserved in both morphologies. High-resolution core-level spectra for Cs 3*d*, Pb 4*f*, and Br 3*d* are displayed in Fig.3(a–c). The characteristic peaks appear at nearly identical binding energies for both QDs and microplates: 738.5 eV and 724.6 eV for Cs $3d_{3/2}$ and Cs $3d_{5/2}$, 142.6 eV and 137.8 eV for Pb $4f_{5/2}$ and Pb $4f_{7/2}$, 69.2 eV and 68.3 eV for Br $3d_{5/2}$ and Br $3d_{3/2}$, respectively. This similarity indicates that there is no significant charge transfer from $CsPbBr_3$ to the ligands or the c-Al_2O_3 substrate. On the other hand, the N 1*s* spectrum of QDs shown in Fig.3(d), broad peaks related to $-NH_3^+$ and $-NH_2$ belonging to OAm are observed at 401.1 eV and 399.2 eV, indicating the presence of ligands on the QDs surface [30,31].

The optical properties of the $CsPbBr_3$ QDs and microplates were investigated using PL spectroscopy with 422 nm laser excitation, and the resulting PL spectra are shown in Fig. 4. The room-temperature PL spectra (Fig. 4(a)) show distinct emission peaks centered at approximately 2.44 and 2.34 eV for QDs and microplates, respectively. The emission peak of the microplates is close to the intrinsic bandgap of bulk $CsPbBr_3$, while the blue-shifted peak observed for the QDs can attributed to quantum confinement effects at the nanoscale [32,33]. The FWHM of the PL peak for the QDs is 78 meV, comparable to values reported for $CsPbBr_3$ QDs synthesized via the hot-injection method [9,34]. By contrast, a smaller FWHM of 63 meV, together with a sharp XRD peaks, is observed for the microplates, suggesting high crystalline uniformity and structural coherence. The higher emission sharpness of the microplates may also be attributed to

reduced exciton–phonon coupling at the surface, resulting from their lower surface-to-volume ratio relative to the QDs [35]. The PLQY of QDs was found to be approximately 75%, which is consistent with the values reported in previous studies [36,37].

Figure 4. (a) PL spectra of $CsPbBr_3$ QDs (black-line) and

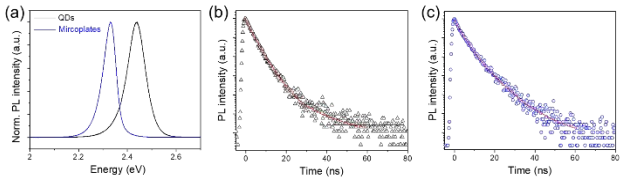

microplates (blue line) excited with 422 nm laser irradiation at room temperature. TRPL spectra of (b) $CsPbBr_3$ QDs and (c) $CsPbBr_3$ microplates.

In contrast, the PLQY of microplates was determined to be about 31%. Despite the fact that microplates exhibit elevated optical properties with narrow bandwidths, the diminished quantum yield may be ascribed due to low quantum confinement effect in large volume, and substantial interaction with the substrate.

PL decay dynamics were analyzed by fitting the TRPL spectra with a biexponential decay model; the fitted curves are shown in Figs. 4(b) and 4(c), and the decay parameters are summarized in Table S1. This model considers both fast and slow recombination processes, and yields fast (τ_1), slow (τ_2), and average (τ_{ave}) lifetimes. For the $CsPbBr_3$ QDs, τ_1, τ_2, and τ_{ave} were determined to be 4.55, 16.47, and 6.78 ns, respectively, whereas for the microplates, the corresponding values were 5.07, 12.38, and 8.11 ns, respectively. The fast decay component is typically associated with radiative recombination of free excitons or surface-related trap-assisted processes, while the slower component reflects carrier recombination through deeper trap states or delayed radiative pathways [38]. The relatively small τ_{ave} values for both QDs and microplates indicate the dominance of radiative recombination over nonradiative processes, suggesting that the samples possess high optical quality. The slightly longer average lifetime of microplates may be attributed to their lower surface-to-volume ratio, which leads to fewer surface traps and hence less nonradiative recombination.

To further investigate the optical characteristics, we performed temperature-dependent PL measurements for both samples over the range of 10 K to 250 K. Previous reports indicate that bulk $CsPbBr_3$ remains structurally stable in the 10–300 K range, while its major phase transitions occur only above 360 K [39]. In nanocrystalline $CsPbBr_3$, however, size and surface effects can stabilize higher-symmetry phases at lower temperatures [15]. Thus, the distinct temperature-dependent optical behaviors observed here may arise not only from morphological differences, but also from differences in temperature-dependent lattice response. As shown in Figs. 5(a) and S3, the PL of the QDs exhibits a slight blueshift in the peak position from 2.32 eV to 2.38 eV and an increase in FWHM from 19.4 meV to 70.6 meV as the temperature increases. The variation in the PL peak position of the QDs near room temperature, apparent in Fig. 5(a), is probably caused by interparticle electronic coupling resulting from solvent removal during the drop-casting process, rather than by intrinsic structural or compositional changes [40]. In Fig. 5(b), the $CsPbBr_3$ microplates exhibit a similar trend, with the emission

Figure 5. Temperature-dependent PL maps for (a) QDs and (b)

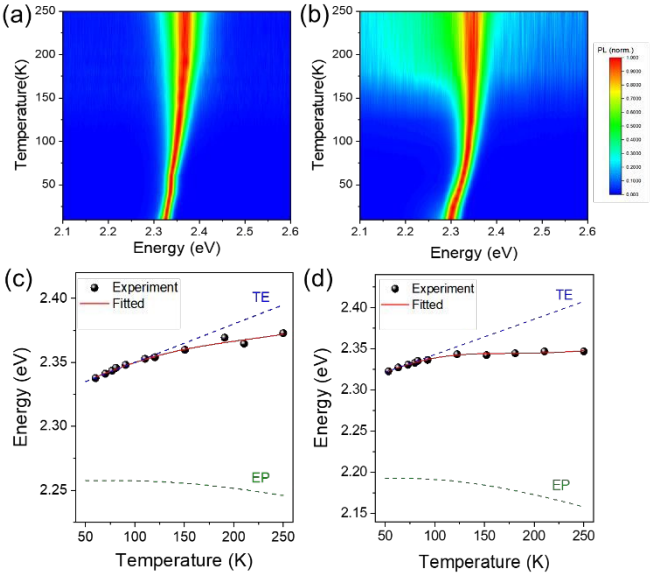

microplates. Calculated contributions from thermal expansion (TE) and electron–phonon (EP) interactions for (c) $CsPbBr_3$ QDs and (d) $CsPbBr_3$ microplates. The solid red line is the fitted curve, and the dashed lines represent the contributions of TE interaction (blue) and EP (green).

peak shifting from 2.29 eV to 2.34 eV and the corresponding FWHM increasing from 28 meV to 65 meV as the temperature increases. Notably, the total variation of the emission peak position for both samples remains within about 50 meV over a temperature range of 240 K, and even shows a slight blueshift. This behaviour represents a significant deviation from the conventional redshift expected from bandgap renormalization in typical semiconductors [41,42]. The weak net bandgap shift and slight blue-shift arise from the competition between thermal expansion and electron–phonon interactions [13,43,44].

As the temperature increases, thermal expansion causes the lattice constants of the crystal to change, leading to modifications in the electronic band structure. Simultaneously, lattice vibrations arising from electron–phonon coupling also influence the electronic band structure. The temperature dependence of the bandgap (E_g) under constant pressure within the framework of the quasi-harmonic approximation can be described as follows [43,44]:

$$\frac{\partial E_g}{\partial T} = \frac{\partial E_g}{\partial V}\frac{\partial V}{\partial T} + \sum_{j,\vec{q}} \left(\frac{\partial E_g}{\partial n_{j,\vec{q}}}\right)\left(n_{j,\vec{q}} + \frac{1}{2}\right) \qquad (1)$$

View Article Online DOI: 10.1039/D5TC04331

where $n_{j,\vec{q}}$ is the number of phonons at the *j* branch with wave vector *q*; $n_{j,\vec{q}}$ follows the Bose–Einstein distribution.

In Equation (1), the first term reflects the impact of lattice thermal expansion, which originates from the anharmonicity of interatomic potentials, and the second term pertains to the effect of electron–phonon interactions on the bandgap. By assuming that the lattice constant is linearly dependent on temperature and by considering a one-oscillator model for phonon interactions, we can simplify Equation (1) as follows [43,44]:

$$E_g(T) = E_0 + A_{TE}T + A_{EP}\left[\frac{2}{exp\left(\frac{\hbar\omega}{k_BT}\right)-1}+1\right] \qquad (2)$$

Here, E_0 denotes the unrenormalized bandgap energy, and A_{TE} and A_{EP} represent the weighting factors for the thermal expansion and electron–phonon interaction contributions, respectively; k_B is Boltzmann's constant, and $\hbar\omega$ is the average optical phonon energy involved in the electron–phonon coupling.

Figures 5(c) and 5(d) show the decoupled contributions of thermal expansion and electron–phonon interactions to the temperature-dependent bandgap variation, obtained by fitting the PL spectra using Eq. (2). The variation of the bandgap with temperature is small for both samples. In both cases, at low temperatures, the bandgap energy is predominantly influenced by thermal expansion, as the population of optical phonon modes is minimal. However, above about 100 K, the activation of optical phonons leads to a redshift in the emission energy. This feature is consistent with previous studies on $CsPbBr_3$ QDs [9,13,45]. Although both samples show similar temperature-dependent trends in their optical behaviour, the absolute magnitudes of the thermal expansion and electron–phonon interactions were different in the two samples. For QDs, the extracted parameters were A_{TE} = 0.03 meV/K and A_{EP} = 62.4 meV. The energy contributions over the 50–250 K range were Δ_{TE} [defined as A_{TE} (250 K) - A_{TE} (50 K)] = 57.0 meV and Δ_{EP} [defined as A_{EP} (250 K) - A_{EP} (50 K)] = -11.8 meV, giving a total shift (Δ_{TE} + Δ_{EP}) was 45.2 meV. For the microplates, we obtained Δ_{TE} = 81.7 meV, Δ_{EP} = - 34.9 meV, and a total shift of 46.8 meV. Clearly, both thermal expansion and electron–phonon interactions are stronger in the nanoplate. For the microplates, there were two main factors contribute to the enhanced thermal expansion interaction. First, in structurally similar perovskites such as $CsSnBr_3$ and $(n\text{-}BA)_2PbI_4$, temperature-induced weakening of the p–s orbital interaction (Sn–Br or Pb–I) leads to an increase in the bandgap energy [26,46,47]. Since the bandgap shift scales with the crystal volume, the larger volume of microplates results in stronger thermal expansion. Second, the strain induced by lattice mismatch and differing thermal expansion coefficients between the perovskite and the substrate strongly influences the energy levels and bandgap modulation of the microplates [48,49]. The lattice mismatch between $CsPbBr_3$ and *c*-Al_2O_3 induces tensile stress owing to the difference in their thermal expansion coefficients (1.2×10^{-4} and 8.1×10^{-6} K^{-1} for $CsPbBr_3$ and c-Al_2O_3, respectively). This typically causes bandgap narrowing of semiconductors with increasing temperature. However, Oksenberg *et al.* reported a blueshift in $CsPbBr_3$ nanowires grown on *c*-Al_2O_3, attributed to lattice rotation and octahedral tilting resulting from heteroepitaxial

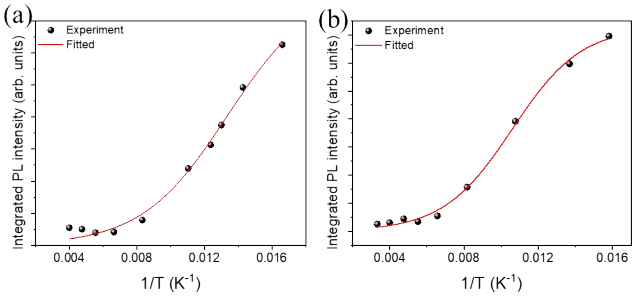

Figure 6. Temperature-dependent integrated PL intensities of (a) $CsPbBr_3$ QDs and (b) $CsPbBr_3$ microplates; the red curves are fits using an Arrhenius-type model.

strain [50]. These structural distortions become more significant as the nanowire height decreases, reducing the Pb–Br–Pb bond angles and thereby increasing the bandgap energy. Accordingly, $CsPbBr_3$ microplates with small height (~100 nm) and large contact area with the substrate can be expected to exhibit stronger thermal expansion interactions. The enhanced electron–phonon interaction in microplates can be attributed to stronger coupling between delocalized carriers and long-range optical phonons; in QDs, spatial confinement limits such interactions [51,52]. Additionally, surface ligands in QDs can further reduce phonon coupling by introducing dielectric screening [53]. In summary, the thermal expansion and electron–phonon interactions in microplates show opposite temperature dependences, partially canceling each other and resulting in only a modest net change in the radiative recombination energy. Finally, the exciton binding energy (E_b) was determined by fitting the temperature-dependent PL intensity using the Arrhenius equation [46],

$$I(T) = \frac{I_0}{1 + Ae^{-E_b/k_BT}} \qquad (3)$$

where I_0 is PL intensity at 0 K and k_B is Boltzmann's constant.

Figure 6 shows the fitted curves used to extract E_b for both $CsPbBr_3$ QDs and microplates. The calculated values of this parameter were 33.86 and 46.31 meV for QDs and microplates, respectively. These values are consistent with previously reported exciton binding energies for $CsPbBr_3$ and, notably exceed the thermal energy at room temperature (~26 meV), suggesting that stable excitonic states can persist under ambient conditions [13,38]. Interestingly, despite the expected enhancement of Coulomb interactions owing to quantum confinement in QDs, which typically leads to higher E_b values, the QDs in this study exhibit a lower exciton binding energy than

the microplates. This counterintuitive result may be attributed to surface-related effects, such as the presence of unstable organic ligands, surface traps, or defects, which can reduce the Coulomb attraction between electrons and holes [54]. The reduced Coulomb attraction lowers the binding energy through the weakening of the electrostatic interaction that holds the exciton together, thereby increasing the likelihood of exciton dissociation. Additionally, the high surface-to-volume ratio in QDs amplifies these effects, further lowering E_b relative to the larger and more highly crystalline nanoplate structures.

Conclusions

A detailed structural and optical comparison of $CsPbBr_3$ quantum dots and microplates reveals significant differences in their temperature-dependent photophysical properties. While both nanostructures exhibit high crystallinity and stable emission, the microplates show narrower PL linewidths, longer exciton lifetimes, and stronger coupling to thermal expansion and phonon interactions. The enhanced interactions in microplates are attributed to their larger crystalline volume, coherent substrate interface, and lower dielectric screening. The insights obtained in this study highlight the complex interplay between dimensional confinement, interface strain, and surface chemistry, and the findings can guide structural engineering strategies for stable, high-performance perovskite optoelectronic devices.

Author contributions

Ga-Eun Kim: Methodology, Formal analysis, Data curation, Writing – original draft. Minjin Kim: Methodology, Formal analysis. Byung Joon Moon: Formal analysis, Data curation. Geol Moon: Investigation, Methodology. Tae-Wook Kim: Methodology, Data curation. Sang-Wan Ryu: Investigation, Methodology. Sang Hyun Lee: Investigation, Data curation, Supervision, Writing – review & editing.

Conflicts of interest

There are no conflicts to declare.

Data availability

The data supporting this article have been included as part of the supplementary information (SI). Supplementary information is available.

Acknowledgements

This study was supported by the Global - Learning & Academic research institution for Master's, PhD students, and Postdocs (LAMP) Program of the National Research Foundation of Korea (NRF), funded by the Ministry of Education (No. Rs-2024-00442775). It was also supported by the Basic Science Research Capacity Enhancement Project through a Korea Basic Science Institute (National Research Facilities and Equipment Center) grant funded by the Ministry of Education (No. RS-2025-02413029).

Notes and references

1 Q.A. Akkerman, G. Rainò, M.V. Kovalenko, and L. Manna, *Nat. Mater.*, 2018, **17**, 394–405. https://doi.org/10.1038/s41563-018-0018-4.
2 Y.P. Fu, H.M. Zhu, J. Chen, M.P. Hautzinger, X.Y. Zhu, and S. Jin, *Nat. Rev. Mater.*, 2019, **4**, 169–188. https://doi.org/10.1038/s41578-019-0080-9.
3 S. Zheng, Z.B. Wang, G.Q. Zheng, H.L. Huang, N.Z. Jiang, Z.H. Zhou, X.M. Wu, T. Pang, L.W. Zeng, R.D. Zhang, F. Huang, D.Q. Chen, *Adv. Funct. Mater.*, 2026, **36**, e21079. https://doi.org/10.1002/adfm.202521079.
4 X.M. Wu, Z.B. Wang, S. Zheng, Z.H. Zhou, R.D. Zhang, L.W. Zeng, F. Huang, D.Q. Chen, *Nano Lett.*, 2025, **25**, 18158–18166. https://doi.org/10.1021/acs.nanolett.5c05743.
5 L. Clinckemalie, D. Valli, M.B.J. Roeffaers, J. Hofkens, B. Pradhan, and E. Debroye, *ACS Energy Lett.*, 2021, **6**, 1290–1314. https://doi.org/10.1021/acsenergylett.1c00007.
6 J.X. Yu, G.X. Liu, C.M. Chen, Y. Li, M.R. Xu, T.L. Wang, G. Zhao, and L. Zhang, *J. Mater. Chem. C*, 2020, **8** 6326–6341. https://doi.org/10.1039/D0TC00922A.
7 A. Dey, P. Rathod, and D. Kabra, *Adv. Opt. Mater.*, 2018, 6, 1800109. https://doi.org/10.1002/adom.201800109.
8 Z.Y. Wu, J. Chen, Y. Mi, X.Y. Sui, S.A. Zhang, W.N. Du, R. Wang, J. Shi, X.X. Wu, X.H. Qiu, Z.Z. Qin, Q. Zhang, and X.F. Liu, *Adv. Opt. Mater.*, 2018, **6**, 1800674. https://doi.org/10.1002/adom.201800674.
9 B.T. Diroll, H. Zhou, and R.D. Schaller, *Adv. Funct. Mater.*, 2018, **28** 1606750. https://doi.org/10.1002/adfm.201606750.
10 T. Ahmed, S. Seth, and A. Samanta, *ACS Nano*, 2019, **13**, 13537–13544. https://doi.org/10.1021/acsnano.9b07471.
11 C.M. Iaru, A. Brodu, N.J.J. van Hoof, S.E.T. ter Huurne, J. Buhot, F. Montanarella, S. Buhbut, P.C.M. Christianen, D. Vanmaekelbergh, C.D. Donega, J.G. Rivas, P.M. Koenraad, and A.Y. Silov, *Nat. Commun.*, 2021, **12**, 5844. https://doi.org/10.1038/s41467-021-26192-0.
12 Q.V. Le, K. Hong, H.W. Jang, and S.Y. Kim, *Adv. Electron. Mater.*, 2018, **4**, 1800335. https://doi.org/10.1002/aelm.201800335.
13 A. Shinde, R. Gahlaut, and S. Mahamuni, Low-Temperature Photoluminescence Studies of $CsPbBr_3$ Quantum Dots, *J. Phys. Chem. C*, 2017, **121** 14872–14878. https://doi.org/10.1021/acs.jpcc.7b02982.
14 Z. Zhao, M.Y. Zhong, W.C. Zhou, Y.H. Peng, Y.L. Yin, D.S. Tang, and B.S. Zou, *J. Phys. Chem. C*, 2019, **123**, 25349–25358. https://doi.org/10.1021/acs.jpcc.9b06643.
15 D.P. Strandell and P. Kambhampati, *J. Phys. Chem. C*, 2021, **125,** 27504–27508. https://doi.org/10.1021/acs.jpcc.1c09501.
16 O.H.C. Cheng, T. Qiao, M. Sheldon, and D.H. Son, *Nanoscale*, 2020, **12** 13113–13118. https://doi.org/10.1039/D0NR02711A.
17 N.K. Kumawat, A. Swarnkar, A. Nag, and D. Kabra, *J. Phys. Chem. C*, 2018, **122**, 13767–13773. https://doi.org/10.1021/acs.jpcc.8b00723.
18 J.T. Zhao, M. Liu, L. Fang, S.L. Jiang, J.T. Zhou, H.Y. Ding, H.W. Huang, W. Wen, Z.L. Luo, Q. Zhang, X.P. Wang, and C. Gao, *J. Phys. Chem. Lett.*, 2017, **8**, 3115–3121. https://doi.org/10.1021/acs.jpclett.7b01083.

19 S. Seth, T. Ahmed, and A. Samanta, *J. Phys. Chem. Lett.*, 2018, **9**, 7007–7014. https://doi.org/10.1021/acs.jpclett.8b02979.

20 X.L. Hu, H. Zhou, Z.Y. Jiang, X. Wang, S.P. Yuan, J.Y. Lan, Y.P. Fu, X.H. Zhang, W.H. Zheng, X.X. Wang, X.L. Zhu, L. Liao, G.Z. Xu, S. Jin, and A.L. Pan, *ACS Nano*, 2017, **11**, 9869–9876. https://doi.org/10.1021/acsnano.7b03660.

21 L.Y. Zhao, Y. Gao, M. Su, Q.Y. Shang, Z. Liu, Q. Li, Q. Wei, M.L. Li, L. Fu, Y.G. Zhong, J. Shi, J. Chen, Y. Zhao, X.H. Qiu, X.F. Liu, N. Tang, G.C. Xing, X.N. Wang, B. Shen, and Q. Zhang, *ACS Nano*, 2019, **13**, 10085–10094. https://doi.org/10.1021/acsnano.9b02885.

22 Z. Su, Z.H. Cao, F.Y. Cao, Y.W. He, J. Zhang, G.E. Weng, X.B. Hu, J.H. Chu, H. Akiyama, and S.Q. Chen, *Chem. Eng. J.*, 2023, **472**, 144906. https://doi.org/10.1016/j.cej.2023.144906.

23 L. Ma, Y.L. Tan, W.C. Zhou, Y.P. Zhao, and Y.C. Wang, *Mater. Lett.*, 2022, **315**, 131931. https://doi.org/10.1016/j.matlet.2022.131931.

24 L. Protesescu, S. Yakunin, M.I. Bodnarchuk, F. Krieg, R. Caputo, C.H. Hendon, R.X. Yang, A. Walsh, and M.V. Kovalenko, *Nano Lett.*, 2015, **15**, 3692–3696. https://doi.org/10.1021/nl5048779.

25 E. Lee, P. Kim, B.J. Moon, H. Lee, S.W. Ryu, Y.I. Park, J.S. Ha, S.H. Lee, *Appl. Surf. Sci.*, 2022, **584** 152575. https://doi.org/10.1016/j.apsusc.2022.152575

26 Y. Li, Z.F. Shi, S. Li, L.Z. Lei, H.F. Ji, D. Wu, T.T. Xu, Y.T. Tian, and X.J. Li, *J. Mater. Chem. C*, 2017, **5**, 8355–8360. https://doi.org/10.1039/C7TC02137B.

27 C.F. Holder and R.E. Schaak, *ACS Nano*, 2019, **13**, 7359–7365. https://doi.org/10.1021/acsnano.9b05157.

28 C. Otero-Martínez, M.L. Zaffalon, Y.P. Ivanov, N. Livakas, L. Goldoni, G. Divitini, S. Bora, G. Saleh, F. Meinardi, A. Fratelli, S. Chakraborty, L. Polavarapu, S. Brovelli, and L. Manna, *ACS Energy Lett.,* 2024, **9**, 2367–2377. https://doi.org/10.1021/acsenergylett.4c00693.

29 A.L. Patterson, *Phys. Rev.,* 1939, **56**, 978. https://doi.org/10.1103/PhysRev.56.978.

30 Y.M. Li, M. Deng, X.Y. Zhang, T. Xu, X.M. Wang, Z.W. Yao, Q.Q. Wang, L. Qian, and C.Y. Xiang, *Nat Commun.*, 2024, **15**, 5696. https://doi.org/10.1038/s41467-024-50022-8.

31 B.H. Liu, A.L. Huang, G.Q. Chen, D. Yang, C.Q. Ma, C. Zhu, L. Li, T.Q. Yang, H. Wu, Y.M. Wu, J.Z. Xu and, H. Gao, *J. Mater. Sci*., 2023, **58**, 16930–16941. https://doi.org/10.1007/s10853-023-09092-0.

32 G. Mannino, I. Deretzis, E. Smecca, A. La Magna, A. Alberti, D. Ceratti, and D. Cahen, *J. Phys. Chem. Lett*., 2020, **11**, 2490–2496. https://doi.org/10.1021/acs.jpclett.0c00295.

33 S.G. Motti, F. Krieg, A.J. Ramadan, J.B. Patel, H.J. Snaith, M.V. Kovalenko, M.B. Johnston, and L.M. Herz, *Adv. Funct. Mater.*, 2020, **30**, 201909904.https://doi.org/10.1002/adfm.201909904.

34 A. Swarnkar, R. Chulliyil, V.K. Ravi, M. Irfanullah, A. Chowdhury, and A. Nag, *Angew. Chem. Int. Edit.*, 2015, **54**, 15424–15428. https://doi.org/10.1002/anie.201508276.

35 J.A. Peters, Z. Liu, O. Bulgin, Y. He, V.V. Klepov, M.C. De Siena, M.G. Kanatzidis, and B.W. Wessels, *J. Phys. Chem. Lett.*, 2021, **12**, 9301–9307. https://doi.org/10.1021/acs.jpclett.1c02397.

36 J. Aneesh, A. Swarnkar, V.K. Ravi, R. Sharma, A. Nag, K.V. Adarsht, *J. Phys. Chem. C*, 2017, **121**, 4734–4739. https://doi.org/10.1021/acs.jpcc.7b00762.

37 G. Jiang, C. Guhrenz, A. Kirch, L. Sonntag, C. Bauer, X.L. Fan, J. Wang, S. Reineke, N. Gaponik, A. Eychmüller, *ACS Nano*, 2019, **13**, 10386–10396. https://doi.org/10.1021/acsnano.9b04179.

38 G. Rainò, M.A. Becker, M.I. Bodnarchuk, R.F. Mahrt, M.V. Kovalenko, and T. Stöferle, *Nature*, 2018, **563**, 671. https://doi.org/10.1038/s41586-018-0683-0.

39 S. Svirskas, S. Balciunas, M. Simenas, G. Usevicius, M. Kinka, M. Velicka, D. Kubicki, M.E. Castillo, A. Karabanov, V.V. Shvartsman, M.D. Soares, V. Sablinskas, A.N. Salak, D.C. Lupascu, J. Banys, *J. Mater. Chem. A*, 2020, **8** 14015–14022. https://doi.org/10.1039/D0TA04155F.

40 Y. Tong, E.P. Yao, A. Manzi, E. Bladt, K. Wang, M. Döblinger, S. Bals, P. Müller-Buschbaum, A.S. Urban, L. Polavarapu, and J. Feldmann, *Adv. Mater.*, 2018, **30**, 1801117. https://doi.org/10.1002/adma.201801117.

41 Y.M. Zhang, Z.Y. Wang, J.Y. Xi, and J. Yang, *J. Phys.-Condens. Mat*., 2020, **32**, 475503. https://doi.org/10.1088/1361-648X/aba45d.

42 P.J. Geng, W.G. Li, X.H. Zhang, X.Y. Zhang, Y. Deng, and H.B. Kou, *J. Phys. D: Appl. Phys*., 2017, **50**, 40LT02. https://doi.org/10.1088/1361-6463/aa85ad.

43 J. Bhosale, A.K. Ramdas, A. Burger, A. Muñoz, A.H. Romero, M. Cardona, R. Lauck, and R.K. Kremer, *Phys. Rev. B*, 2012, **86** 195208. https://doi.org/10.1103/PhysRevB.86.195208.

44 C.L. Yu, Z. Chen, J.J. Wang, W. Pfenninger, N. Vockic, J.T. Kenney, and K. Shum, *J. Appl. Phys*., 2011, **110**, 063526. https://doi.org/10.1063/1.3638699.

45 X.Z. Zhou and Z.Y. Zhang, *AIP Adv.*, 2020, **10**, 125015. https://doi.org/10.1063/5.0017149.

46 L.Y. Huang, and W.R.L. Lambrecht, *Phys. Rev. B*, 2013, **88**, 165203. https://doi.org/10.1103/PhysRevB.88.165203.

47 S. Wang, J.Q. Ma, W.C. Li, J. Wang, H.Z. Wang, H.Z. Shen, J.Z. Li, J.Q. Wang, H.M. Luo, and D.H. Li, *J. Phys. Chem. Lett*., 2019, **10**, 2546–2553. https://doi.org/10.1021/acs.jpclett.9b01011.

48 Y.A. Jiao, S.H. Yi, H.W. Wang, B. Li, W.Z. Hao, L.L. Pan, Y. Shi, X.Y. Li, P.F. Liu, H. Zhang, C.F. Gao, J.J. Zhao, and J. Lu, *Adv. Funct. Mater*., 2021, **31**, 2006243. https://doi.org/10.1002/adfm.202006243.

49 Y.M. Chen, Y.S. Lei, Y.H. Li, Y.G. Yu, J.Z. Cai, M.H. Chiu, R. Rao, Y. Gu, C.F. Wang, W.J. Choi, H.J. Hu, C.H. Wang, Y. Li, J.W. Song, J.X. Zhang, B.Y. Qi, M.Y. Lin, Z.R. Zhang, A.E. Islam, B. Maruyama, S. Dayeh, L.J. Li, K.S. Yang, Y.H. Lo, and S. Xu, Nature, 2020, **577**, 209-215. https://doi.org/10.1038/s41586-019-1868-x.

50 E. Oksenberg, A. Merdasa, L. Houben, I. Kaplan-Ashiri, A. Rothman, I.G. Scheblykin, E.L. Unger, and E. Joselevich, *Nat. Commun.*, 2020, **11**, 489. https://doi.org/10.1038/s41467-020-14365-2.

51 R.P. Wang, G. Xu, and P. Jin, *Phys. Rev. B*, 2004, **69**, 113303. https://doi.org/10.1103/PhysRevB.69.113303.

52 C.L. Zhu, L.G. Feld, M. Svyrydenko, I. Cherniukh, D.N. Dirin, M.I. Bodnarchuk, V. Wood, N. Yazdani, S.C. Boehme, M.V. Kovalenko, and G. Rainò, *Adv. Opt. Mater.*, 2024, **12**, 2301534. https://doi.org/10.1002/adom.202301534.

53 R. Su, Z.J. Xu, J. Wu, D.Y. Luo, Q. Hu, W.Q. Yang, X.Y. Yang, R.P. Zhang, H.Y. Yu, T.P. Russell, Q.H. Gong, W. Zhang, and R. Zhu, *Nat. Commun.*, 2021, *12*, 2479. https://doi.org/10.1038/s41467-021-22783-z.

54 F.Y. Zhong, J.P. Sheng, C.Y. Du, Y. He, Y.J. Sun, and F. Dong, *Sci. Bull*., 2024, **69**, 901–912. https://doi.org/10.1016/j.scib.2024.01.027.

View Article Online
DOI: 10.1039/D5TC04393J

View Article Online
DOI: 10.1039/D5TC04393J

The data supporting this article have been included as part of the Supplementary Information.

Supplementary information: Additional TEM, SEM, temperature PL and TRPL data (Fig. S1, Fig. S2, Fig. S3, and Table S1.)